



HAL
open science

The use of hat-shaped specimens to study the high strain rate shear behaviour of Ti-6Al-4V

J. Peirs, U.P. Verleysen, J. Degrieck, F. Coghe

► **To cite this version:**

J. Peirs, U.P. Verleysen, J. Degrieck, F. Coghe. The use of hat-shaped specimens to study the high strain rate shear behaviour of Ti-6Al-4V. *International Journal of Impact Engineering*, 2010, 37 (6), pp.703. 10.1016/j.ijimpeng.2009.08.002 . hal-00674106

HAL Id: hal-00674106

<https://hal.science/hal-00674106>

Submitted on 25 Feb 2012

HAL is a multi-disciplinary open access archive for the deposit and dissemination of scientific research documents, whether they are published or not. The documents may come from teaching and research institutions in France or abroad, or from public or private research centers.

L'archive ouverte pluridisciplinaire **HAL**, est destinée au dépôt et à la diffusion de documents scientifiques de niveau recherche, publiés ou non, émanant des établissements d'enseignement et de recherche français ou étrangers, des laboratoires publics ou privés.

Accepted Manuscript

Title: The use of hat-shaped specimens to study the high strain rate shear behaviour of Ti-6Al-4V

Authors: J. Peirs, U.P. Verleysen, J. Degrieck, F. Coghe

PII: S0734-743X(09)00144-4

DOI: [10.1016/j.ijimpeng.2009.08.002](https://doi.org/10.1016/j.ijimpeng.2009.08.002)

Reference: IE 1823

To appear in: *International Journal of Impact Engineering*

Received Date: 30 November 2008

Revised Date: 10 August 2009

Accepted Date: 11 August 2009

Please cite this article as: Peirs J, Verleysen UP, Degrieck J, Coghe F. The use of hat-shaped specimens to study the high strain rate shear behaviour of Ti-6Al-4V, *International Journal of Impact Engineering* (2009), doi: 10.1016/j.ijimpeng.2009.08.002

This is a PDF file of an unedited manuscript that has been accepted for publication. As a service to our customers we are providing this early version of the manuscript. The manuscript will undergo copyediting, typesetting, and review of the resulting proof before it is published in its final form. Please note that during the production process errors may be discovered which could affect the content, and all legal disclaimers that apply to the journal pertain.



The use of hat-shaped specimens to study the high strain rate shear behaviour of Ti-6Al-4V

J. Peirs¹, P. Verleysen¹, J. Degrieck¹ and F. Coghe²

¹*Ghent University, Faculty of Engineering, Materials Science and Engineering, Gent, Belgium;* ²*Royal Military Academy, Dept. of Civil and Materials Engineering, Brussels, Belgium*

Abstract

To study the high strain rate shear behaviour of Ti-6Al-4V, hat-shaped specimens have been used in a compression split Hopkinson bar setup. With this technique, highly concentrated shear strains are obtained which eventually cause strain localization and adiabatic shear bands (ASB). Because of the complex stress distribution in the specimen, interpretation of the experimental results is not straightforward. In this paper, results of a comprehensive experimental and numerical study are presented, aiming at a more judicious use of hat-shaped specimens and a fundamental understanding of the obtained results. Specimens with different dimensions are considered. It is found that the width of the shear region and the radius of the corners are the most important parameters. The first mainly affects the homogeneity of stresses and deformations in the shear zone and the presence of a hydrostatic stress next to the shear stress, while the latter primarily governs the initiation of the ASB. The relation between the global measured response and the local material behaviour is studied. It is shown that, within certain limits, the shear stress in the shear region can be extracted from the measured force. Several experiments which have been interrupted at a certain level of deformation have been carried out. The microstructure could thus be observed at different stages: onset of strain localization, formation of ASBs, initiation and propagation of microcracks.

Keywords: adiabatic shear band, titanium alloy, Ti-6Al-4V, Hopkinson, high strain rate, hat-shaped specimen, finite elements, fracture

1. Introduction

Shear testing is an obvious way to study the mechanical behaviour of metals because metals basically deform plastically by shear. Moreover, in practical applications materials are often dynamically loaded

directly in shear (punching, machining, impact...). In these loading cases, deformation can become unstable leading to the formation of adiabatic shear bands (ASB), followed by fracture.

Adiabatic Shear Bands (ASBs) are a thermodynamic phenomenon during which large deformations are observed in a narrow band (typically $5\mu\text{m}$ to $100\mu\text{m}$) of the material at high strain-rates. Although the main mechanism for adiabatic shearing is the competition between strain hardening and thermal softening, the whole process is very complex and involves high temperatures, high strain-rates, high strains, high strain gradients, material transformations, etc. The formation of ASBs is not a failure mode as such but it causes the material to lose its load carrying and energy absorption capacity [1]. Since adiabatic shearing is known to be a precursor to failure, it is important to understand the whole process which starts with strain localization and finally ends up with failure. Adiabatic shear bands are observed in many applications such as machine chips, forging and ballistic impact loading. In most cases the occurrence of adiabatic shearing is undesirable, yet recently developed adiabatic cutting and blanking techniques use this phenomenon in their advantage.

Through many years, engineers have developed several experimental techniques to study the dynamic shear behaviour of materials, including the formation of adiabatic shear bands and fracture. The present study deals with a technique which makes use of hat-shaped specimens, dynamically compressed in a split Hopkinson pressure bar set-up. Due to the specific geometry of the specimen, a zone where the material is mainly deformed in shear exists. Even materials that do not show strain localization spontaneously can be forced up to shearing failure. Hat-shaped specimens were originally proposed by Meyer and Manwaring in 1986 [2] and were recently used by Bronkhorst to study shear localization in tantalum and 316L stainless steel [3]. Tantalum was also studied by Nemat-Nasser [4]. Although both researchers did similar experiments, other specimen dimensions were used, resulting in differences in the observed behaviour. Results presented in Kad et al. [5], Meyers et al [6], Beatty et al. [7], Couque et al. [8], Longère et al. [9] confirm that the outcome of experiments is not only affected by the tested material but also by the specimen geometry. Hence, results from different studies must be compared with great care.

Extracting quantitative data on the material behaviour from tests on hat-shaped specimens is not straightforward because of the complex stress and deformation distribution in the shearing region. Since the shear band develops subsurface, it is impossible to track the shear band, detect its temperature and measure the local strain. More insight in the response of the shearing zone to the

imposed deformation is needed in order to better understand the experimental data obtained by this technique. As the nucleation and propagation of ASBs depends on the stress condition [10], knowledge of the stress distribution in the specimen is crucial. In a further step, knowledge of the relation between specimen geometry and stress state can be exploited for an in-depth study of the shear band nucleation and propagation [8]. Indeed, it appears that normal, compressive stress and hydrostatic pressure both delay shear fracture. Yet it is still unclear how these stresses affect the susceptibility of materials to adiabatic shear banding [1]. Altering the specimen geometry, and consequently the stress state in the shearing zone, allows to study the effect of these stress components.

One of the goals of this contribution is to gain deeper insight into this interesting experimental technique and to relate the specimen dimensions with the stress and strain distribution and evolution within the hat-shaped specimen. In addition, the existence of an optimal specimen geometry to achieve an as pure as possible shearing stress state, is studied. Numerical simulations based on the finite element (FE) method are used for these purposes. Several slightly different geometries are simulated to study the relation between the geometry and the global and local behaviour of the specimen. In particular, the possibility to retrieve information about the local shearing process (stress and strain) from the signals recorded on the Hopkinson bars is studied. Attention is paid to the stress and strain homogeneity.

Next to the extensive simulation program, quasi-static and dynamic experiments are carried out on a series of hat-shaped specimens of a Ti-6Al-4V alloy. This material was chosen because, due to its low mass density and heat conductivity, Ti-6Al-4V is very sensitive to the formation of adiabatic shear bands [1, 11-16]. Ti-6Al-4V is the most commonly used titanium alloy. A lot of research has already been conducted on adiabatic shear banding and failure in this material. Several dynamic experimental techniques have been used: shear compression specimen test (SCS) [15], torsion of thin walled tubes [16], thick-walled cylinder implosion test [17], modified double shear test [18], impact on a plate [19], etc. A common feature of these experiments is that the specimen is deformed until either the material fails or the energy of the impact is fully absorbed, since interrupting the experiment at a certain level of deformation it is not obvious. Experiments using hat-shaped specimens however, are easy to interrupt by the use of a stopper ring.

The experiments presented here are interrupted at different strain levels and the microstructure of the deformed material is studied. Information of the failure process at different stages, from an adiabatic

shear band towards fracture, is thus obtained [6, 20]. The experimentally observed fracture process is compared with the numerical results.

2. Experiments

2.1. Experimental method and material

The split Hopkinson pressure bar technique is used to load the specimens dynamically. The small specimen is placed between two Hopkinson bars (Figure 1). A compressive loading wave ϵ_i , generated in the input bar by impact of a projectile, propagates along the bar towards the specimen. This wave interacts with the specimen and is partly reflected back into the input bar (ϵ_r) and partly transmitted into the output bar (ϵ_t). These three waves (ϵ_i , ϵ_r and ϵ_t) are measured by means of strain gages on the Hopkinson bars. From those waves, the total force and the global deformation of the specimen can be determined, based on the principles of one-dimensional elastic-wave propagation in slender bars [21]. The set-up used in this study has aluminium (Al5083) bars with lengths of 6m and 3m, and a diameter of 25mm.

Figure 1: Sketch of a split Hopkinson pressure bar set-up

In an axi-symmetric hat-shaped specimen, shear strains are concentrated in a narrow zone.

Figure 2 shows the specimen between the two Hopkinson bars. The specimen can be divided into three regions: the upper *hat* part, the lower *brim* part and the *shear* region where high shear strains develop. Grease is used to stick the specimen between the bars and to reduce friction. Deformation of the specimen can be limited to a certain level by means of a stopper ring (SR). Figure 3 provides the dimensions of the specimen used in this study. These dimensions were selected on the basis of a literature review (Table 1) and further optimized by numerical simulations (§3).

The specimens are carefully machined out of a standard extruded Ti-6Al-4V bar in the mill-annealed condition with a diameter of 16mm. The specimen production process consists of turning the outer shape of the specimen, followed by drilling the hole in the specimen. The alloy consists of a majority of hexagonal (HCP) α -phase (97%) and a finely dispersed cubic (BCC) β -phase (3%). The chemical composition of the material used in the experiments was determined by Coghe [11]: Al 6.28 wt%, V 4.18 wt%, Fe 0.18 wt% and O <0.2wt%.

Figure 2: Hat-shaped specimen between Hopkinson bars. Arrows represent the displacement direction.

Figure 3: Specimen dimensions: $r_1=4.0\text{mm}$, $r_2=4.1\text{mm}$, $r_3=8\text{mm}$, $h_1=4.0\text{mm}$, $h_2=5.0\text{mm}$ and $h_3=8.0\text{mm}$, with indication of the ‘shear region centre’. The figure is taken from [3].

Table 1: Dimensions of hat-shaped specimens used in literature (mm)

Source	r_1	r_2	r_1/r_2	r_3	h_1	h_2	h_2-h_1	h_3
Bronkhorst et. al. [3]	2.09	2.28	0.92	4.30	2.60	3.47	0.87	5.11
Nemat-Nasser et. al. [4]	4.31	4.44	0.97	6.35	3.30	4.55	1.25	7.85
Kad et. al. [5]	4.99	5.08	0.98	9.55	4.80	-	-	10.00
Beatty et. al. [7]	4.76	4.76	1	9.53	4.75	5.97	1.22	11.81
Couque et. al. [8]	6.2	7.8	0.8	10	7	9.5	2.5	15.5
Lins et. al.[20]	4.85	5.08	0.95	9.53	6.97	8.00	1.03	15.00
Lee et. al. [22]	4	4.05	0.99	-	3.5	5.5	2	8.5

Because all plastic deformation occurs in the shearing region, the indentation of the hat into the brim at time t can be calculated with a good approximation as the top-to-bottom surface displacement of the sample Δu . The small dimensions of the specimen ensure that force equilibrium is established very soon after onset of loading. Here both aluminium bars have the same diameter, consequently: $\varepsilon_t = \varepsilon_i + \varepsilon_r$, making equation 2.1 valid [21].

$$\Delta u = 2C_b \int_0^t \varepsilon_r dt \quad (2.1)$$

with ε_r the reflected wave and C_b the longitudinal wave speed in the bars. The shear strain γ can only be roughly estimated from Δu because the width of the shear region and the strain distribution in the shear region are not known (see §4.3).

Because of the force equilibrium in the specimen, the total axial load on the specimen can be determined from the transmitted wave ε_t by

$$F_a = A_b E_b \varepsilon_t \quad (2.2)$$

with A_b the sectional area and E_b the elasticity modulus of the Hopkinson bars. The shear stress in the shear region can be estimated quite accurately for the used specimen geometry by dividing the axial

force (according to 2.2) by the surface of the shear region $A_{SR} = \pi(r_1 + r_2)(h_2 - h_1)$: $\tau = \frac{F_a}{A_{SR}}$. As

will be shown (§4.3), a slight overestimation of the shear stress is obtained.

2.2. Experimental results

Ten hat-shaped specimens have been produced with the dimensions shown in Table 2. The radius of the hole in the brim is always 4.0mm while there are small variations on the outer diameter. Only the radius of the outer corner (R) could be measured. Variations of R along the circumference of the specimen cannot be excluded.

Table 2: Measured dimensions of the produced specimens. The < sign means that corner is sharp.

	Exp1	Exp2	Exp3	Exp4	Exp5	Exp6	Exp7	Exp8	Exp9	Exp10
r_1/r_2	0.98	0.99	0.96	0.97	0.98	1.000	0.98	0.98	0.98	0.98
$H=h_2-h_1$ (mm)	1.15	1.10	1.10	1.00	1.00	1.05	1.05	1.10	1.00	1.00
R (mm)	<	<	0.03	<	0.04	0.05	0.06	0.02	0.03	<

Dynamic (Exp1-Exp9) and quasi-static experiments (Exp10) have been carried out on these samples. The average displacement velocity was 0.083mm/s in the quasi-static experiment. In the dynamic experiments approximately 1500mm/s is reached before localization, after localization the displacement velocity increases, up to more than 3000mm/s. The average shear stress in the shear region is calculated by dividing the applied force (eq. 2.2) by the area of the shear region A_{SR} .

The resulting stress-displacement curves of the dynamic experiments are presented in Figure 4. The deformation of Exp4-Exp7 is interrupted after reaching maximum force while Exp8 and Exp9 are interrupted before. Although, all curves have a similar shape, closer examination learns that the maximum stress for Exp1 and Exp6 is not only higher, but the value (± 820 MPa) is also longer maintained. For the other specimens, the stress drops abruptly after reaching maximum stress. Peak shear stresses vary between 670MPa and 820MPa and occur at displacements between 0.11mm and 0.16mm. The scatter can partly be attributed to variations in specimen dimensions. However, the variations in experimental results are not always in agreement with the expected variations due to the specimen geometry. There is for example no particular variation in the dimensions (Table 2) explaining the different behaviour of Exp 1 and Exp 6 compared with the other experiments. It is therefore assumed that imperfections in the rounding of the specimen corners are responsible. This is confirmed by the simulations (section 4.2). In addition, scatter in deformation values is also due to a bad contact between the bars and the specimen at the onset of loading because of the grease which is used.

Figure 4: Stress-displacement curves of the dynamic experiments Exp1-Exp9

Typical stress-displacement curves of a dynamic and static experiment are compared in Figure 5. The dynamic stress-displacement curve shows a peak in the force while in the quasi-static loading case the force stays on a constant level, even after fracture. During the quasi-static experiment, there is enough time for the heat to be conducted away from the shear region, which prevents thermal softening. This explains the completely different behaviour of a statically loaded titanium specimen compared with a dynamically loaded one.

As mentioned before, the formation of an adiabatic shear band is not a failure mode as such. However, it can lead to failure. The whole deformation process exists of different steps, which can be studied with experiments, interrupted at different levels of strain. The points at which the experiments were interrupted are indicated with arrows in Figure 5. The following part describes the different steps (1-5) and illustrates them with microscopic images. Sometimes, different steps in the evolution towards fracture can be found in one sample. Although the specimen is axi-symmetric, the deformation of the specimen and the shear band are three dimensional. The finite element simulations in the next section are used for interpretation of the experimental observations.

Figure 5: Stress-displacement curves of a typical dynamic (Exp1) and quasi-static experiment (Exp10).

The arrows indicate the displacements where other dynamic experiments were interrupted.

Shear strain concentration (step 1 – Exp8)

It is generally accepted that adiabatic shear bands initiate at a material discontinuity or geometrical imperfection. In the hat-shaped specimen, the corners of the specimen form initiation locations for strain localization. High strains are indeed found in the corners of the specimen from Exp8. There is only limited deformation in the centre of the shear region. The radius of the corners plays of course an important role in this first step.

Shear band formation and initiation of multiple micro-cracks (steps 2 and 3 – Exp9 and Exp7)

Higher temperatures are reached where the strain concentrates resulting in thermal softening and further strain localization causing even higher temperatures and more strain localization (step 2). Temperatures up to 1100°C have been experimentally observed [23, 24] and are also obtained in the simulations of this study (§4.1). This instable process starts at the initiation places (step 1) and expands very rapidly until a fully developed shear band stretches out from corner to corner in the hat-shaped

specimen (Figure 6). The shear bands that are formed in Ti-6Al-4V are very narrow ($5\mu\text{m}$ - $10\mu\text{m}$). Because of the large strains, individual grains can hardly be distinguished in the shear band.

Figure 6: LOM image of fully developed adiabatic shear band (Exp7); the arrows show the direction of the displacement

Meanwhile, cracks in the shear region are formed not only at the corners (Figure 7b) but also at other locations along the shear band (Figure 7c). The initiation of cracks at different places can possibly be related with the so-called hot-spots which have been observed along fully developed shear bands, in an experimental [25] and numerical [26] way. Numerical simulations in this study also revealed a periodic temperature and hydrostatic pressure field (see §4.1). The turbulent temperature field can be related with the formation of multiple cracks.

Figure 7: Schematic representation and LOM micrographs of fracture process: a) grains are initially approximated to circles; b) deformation causes grains to elongate and rotate; micro-cracks with the same orientation as the grains are formed (Exp9); c) several micro-cracks are linked, the resulting crack surface looks fragmented. Twins are observed in the vicinity of the shear band.

The orientation of the cracks is coincident with the orientation of the highly deformed grains and this direction is not the same as the direction of the shear band; the cracks traverse the shear band. This can be seen in Figure 7b which shows micro-cracks in the vicinity of the tip of the large crack at the corner. However, the axis of the cracks gradually rotates towards the shear line.

Linkage of the micro-cracks (step 4 – Exp4, 5, 6)

Several small micro-cracks rotate and are linked to form larger cracks by a process similar to void growth and coalescence. This results in cracks with a ‘wavy’ crack surface (Figure 8 and Figure 7c). The typical void growth and coalescence pattern is clearly observed at the corners of the specimen but also at other locations along the shear line. Figure 7 illustrates schematically the observed crack growth. Deformation twins in the vicinity of the shear band are also indicated on Figure 7c.

Figure 8: LOM image of specimen with deformation limited to 0.2mm by a stopper ring. The crack at the corner of the specimen is clearly formed by a process of void growth and coalescence (Exp9).

Melting and welding of the material (step 5 – Exp1, 2 and 3)

High temperatures are reached in the Ti-6Al-4V. If the specimen is further deformed after fracture, the temperature keeps on rising because of friction between the crack surfaces, eventually leading to melting of the material. Also the hydrostatic pressure increases when the deformation increases. The combination of high temperatures and hydrostatic pressure closes the cracks formed in step 4. Indeed, experimentally, structures are observed which resemble molten material and cracks disappear because the fracture surfaces are “welded” together. The welds, which seem to be a little bit wider than the original shear band (10 μ m-30 μ m), can be confused with the original shear bands, yet they have another origin. Welding was observed after indentations above approximately 0.35mm. This process is important because it determines the residual strength of the component after failure. It should be noticed that the microstructure observed after an experiment is not necessarily the same as the microstructure at the end of the deformation. At the end of the deformation, very high cooling rates exist. Indeed, despite the low heat conductivity of the titanium, the mass of the heated material is very small and temperature gradients are high.

3. Numerical simulations

To obtain an in-depth understanding of the experimental results and, subsequently, improvement of the experiments, numerical FE simulations are performed. These simulations do not intend to exactly reproduce the behaviour of one particular material (Ti-6Al-4V) or to study the adiabatic shear bands itself. With the simulations detailed information about the response of the hat-shaped specimen is obtained. Consequently, the minimal requirement for the FE-model is that thermal softening and localization are correctly predicted.

A 2D axi-symmetric model of the titanium specimen is defined in ABAQUS/Explicit. The dimensions of the initial model are given in Figure 3. Variations on these dimensions have also been used as indicated in §4.2. A uniform velocity is imposed to the top-face of the specimen: after a rise time of 20 μ s, the top-face is moving at a constant velocity of 5m/s in the axial direction. The bottom-face is fixed in the axial direction but is free to move in the radial direction in order to simulate a frictionless contact (grease) with the Hopkinson bar.

For the specimen material a classical metal, elasto-plasticity model with isotropic hardening is used. The Johnson-Cook (JC) model is used to describe the effect of the strain hardening, strain-rate ($\dot{\epsilon}$) hardening and temperature softening on the stress σ [27, 28]:

$$\sigma = \left[A + B \varepsilon_p^n \right] \left[1 + C \ln \frac{\dot{\varepsilon}}{\dot{\varepsilon}_0} \right] \left[1 - \left(\frac{T - T_{room}}{T_{melt} - T_{room}} \right)^m \right] \quad (3.1)$$

where ε_p is the plastic strain, $\dot{\varepsilon}_0$ is a reference value of the strain rate, T the temperature, T_{melt} the melting temperature and T_{room} is the room temperature. A , B , C , n and m are material parameters with C describing the materials strain-rate dependency. The parameters were determined by means of compression tests [11]. Lee and Lin [13] showed that one set of JC parameters is sufficient to describe the behaviour of Ti-6Al-4V in a wide range of temperatures from room temperature up to 1100°C. Thus, even above the β -transition temperature, the Johnson-Cook model can still be used.

Heat is generated by the plastic work of the material. The resulting temperature increase for an adiabatic process can be estimated by integration of the energy dissipated by the plastic work:

$$\Delta T = \beta \frac{1}{\rho c} \int \sigma d\varepsilon \quad (3.2)$$

where ρ and c are the mass density and specific heat of the material respectively. In the simulations, the specific heat c is assumed to be independent of the temperature. The Taylor-Quinney coefficient β is assumed to have a constant value of 0.9. Although this is an acceptable approximation in the scope of this study [1], recent work by Rosakis et al. [29] and Longere et al. [30] shows that this can introduce errors. Heat conduction is also included in the model. Temperature dependence of the heat conductivity k (W/mK) is neglected and a constant value is used. Table 3 summarizes the values of the parameters used in the model.

Table 3: Material parameters used for Ti-6Al-4V in the numerical simulations

A (MPa)	B (MPa)	C	m	n	$\dot{\varepsilon}_0$ (s ⁻¹)	β
1120	667	0.0270	1.33	0.47	1	0.9
T_{melt} (°C)	T_{room} (°C)	ρ (kg/m ³)	c (J/kg K)	E (GPa)	ν	k (W/m K)
1653	20	4428	580	114	0.3	6.70

4-node bilinear axi-symmetric quadrilateral elements with reduced integration (CAX4R) are used. Small elements are necessary, to avoid element-averaging effects [10] and to capture initiation and nucleation of the ASB. The elements in the shearing region of the specimen (Figure 9) are rectangles with a width of 15 μ m and a height of 20 μ m. Rectangular elements perform better than square elements,

since during compression they come close to squares. The rate-dependency of the material model is not sufficient to avoid mesh sensitivity. Refining the mesh does not lead up to a unique solution. Several researchers have proposed methods to lower mesh dependency [31-33]. In this study, mesh sensitivity problems are by-passed by using the same mesh in each simulation.

Figure 9: Illustration of ABAQUS/Explicit finite element model showing the mesh and boundary conditions used in all simulations. Different variants for the geometry have been used.

ALE adaptive meshing is used to avoid extensive element distortion. Elements are not created or deleted but rearranged. The large deformation also causes elements at the edge of the hat and the brim to make contact. These contact interactions are modelled as frictionless kinematic contact pairs.

With this model the previously stated requirement for the performance of the FE simulations is met. As can be seen on Figure 10a, thermal softening and strain localization in the dynamic experiments are predicted by the simulation. As a first approximation, strain localization is assumed to begin when the stress decreases for increasing strain. The same model is used for the static simulation, only the displacement speed is reduced to 0.0833mm/s. Conductive heat transfer prevents thermal softening and strain localization in the static simulations and, since no material damage is implemented in the model, the force is not decreasing. Comparison with the experiments (Figure 10b) learns that the trends are correctly represented in the simulation. The absence of a damage model in the simulations can explain the discrepancy between the experimental and simulated static behaviour.

Figure 10: Comparison of dynamic and static force-displacement curves from FE simulations and experiments with the same specimen geometry

4. Discussion

4.1. Stress composition

Although hat-shaped specimens are primarily used to investigate the shear behaviour of materials, also normal stresses exist in the shear region. Figure 11 represents the shear stress σ_{rz} , the radial stress σ_r and the axial stress σ_{zz} in the centre of the shear region of a specimen with dimensions given in Figure 3 (see caption) for a dynamic simulation. The normal, compressive stresses are clearly non-negligible and eventually exceed the shear stress after the formation of a shear band (displacement > 0.2mm). If further deformed after the maximum load, the material loses its load carrying capacity and the top of the hat is driven as a wedge into the brim.

Figure 11: Stress composition in the centre of the shear region for a specimen with the dimensions of figure 3: shear stress σ_{rz} , normal radial stress σ_{rr} and axial stress σ_{zz}

The stress distribution has also been investigated for specimens with other dimensions than the one of Figure 3. It is found that a pure shear and homogeneous stress state in the shear zone cannot be obtained simultaneously in hat-shaped specimens.

The relation between the stress components σ_{rr} , σ_{zz} and σ_{rz} is presented in Mohr's circle in Figure 12 at three different moments: before localization (displacement 0.05mm), during localization (0.15mm) and finally when a shear band (0.35mm) has fully developed. Normal stresses are depicted on the horizontal axis, shear stresses on the vertical axis. Line r-z corresponds with the stress state in a coordinate system where the r-axis has a radial orientation and the z-axis an axial orientation. Two additional lines can be found on the circle: the vertical one represents the orientation of the maximal shear stress; the dotted line represents the direction of the line connecting the two corners of the specimens shear region. The lines clearly do not coincide. From Figure 12 it is clear that both the orientation of the maximal shear stress and the in-plane hydrostatic pressure (corresponding with the centre of the circle) vary during the experiment. At the onset of loading, the plane where maximal shear stress occurs makes an angle of 18° with the axial direction. This angle decreases until maximal shear stress occurs in the plane between the corners of the specimen when the shear band starts to form. This explains the experimentally observed rotation of the grains. The second parameter, the hydrostatic pressure, increases during the experiment and high pressures up to 3GPa are reached at a displacement of 0.35mm. Hydrostatic pressure affects the formation of adiabatic shear bands [8]. Moreover, high hydrostatic pressure prevents voids to grow and will consequently retard failure of the specimen. Furthermore, in the beginning of the experiment the major principal stress σ_1 is positive (tensile) while at the end of the experiment σ_1 becomes negative (pressure). This also affects the formation and propagation of cracks in the specimen.

Figure 12: Stress state in the centre of the shear region represented by means of Mohr's circle at three different moments: before localization ($20\mu\text{s}$), during localization ($40\mu\text{s}$) and at a fully developed shear band ($80\mu\text{s}$)

Figure 13 shows the distribution of the hydrostatic pressure and temperature along the shear line at $40\mu\text{s}$ (onset of ASB) and $80\mu\text{s}$ (fully developed shear band). The temperature is more homogeneous than the pressure. Their distribution evolves during the deformation process: at $40\mu\text{s}$ both pressure and temperature are lower around the centre of the shear region, at the end higher. The pressure distribution affects the formation of cracks as is confirmed by experimental observations showing that cracks are typically located at the corners where hydrostatic stresses are the lowest. However, when observing specimens of experiments interrupted at low levels of deformation, cracks are also seen in the centre of the shear band. This is in agreement with the low hydrostatic pressure around the centre seen at $40\mu\text{s}$. Moreover, these cracks seem to disappear in more heavily deformed specimens what can be explained by the higher pressure reached. At $80\mu\text{s}$ both the pressure and the temperature show peak values at periodic positions. Although, the distance between the peaks of approximately $100\mu\text{m}$ is much higher than the size of the elements, the peaks originate from the mesh. In the simulation, the behaviour of a point of the shear band which coincides with a node of the mesh is evaluated in a different way than for a point which does not coincide with a node. The temperature peaks are numerical instabilities but they resemble to the physical phenomenon of the so-called hot-spots, experimentally observed by Guduru [25]. Since stress, strain and temperature are not constant along the shear band, local thermodynamic instabilities can occur within the shear band. These physical instabilities can be compared with an unstable plane Couette flow in fluids [26]. The periodic hot-spots can be initiation places for cracks.

Figure 13: Hydrostatic pressure and temperature distribution along the shear line at two different moments for a specimen with dimensions of Figure 3.

4.2. Influence of the specimen geometry

To relate characteristic dimensions of the specimen to the global response and stress state in the specimen, five series of simulations, have been performed, each with a different dimension being

varied (Figure 3): the width of the shear region characterized by r_1/r_2 (1), the height of the shear region h_2-h_1 (2), the radius of the corners R (3), the outer diameter r_3 (4) and the depth of the hole h_1 (5). From the simulations it was clear that only the first three have a non-negligible effect.

Width of the shear region

A ratio r_1/r_2 less than 1 means that the outer diameter of the hat is larger than the inner diameter of the hole in the brim. This is the case for most specimens found in literature [3-5, 8, 20]. Six simulations with r_1/r_2 ratios varying from 1.05 to 0.9 are performed. The height of the shear region is 1mm for all specimens and the corners are not rounded. The resulting force-displacement curves are shown in Figure 14.

As can be seen from Figure 14, changes in r_1/r_2 result in large differences in the observed specimen behaviour, however all curves show the same evolution: after a linear part, the force very soon increases much slower, to reach a peak, after which the force drops. The following conclusions can be drawn:

- The further away r_1/r_2 is from one, the higher the force needed to deform the specimen. This is due to both the higher hydrostatic pressure and the fact that more material is involved in the shear process in specimens. As a consequence, the deformation energy is larger for specimens with low r_1/r_2 ratio.
- The displacement at which the peak force occurs is higher for specimens with low r_1/r_2 , values. The shear strain, however, remains the same. Consequently, the relation between the indentation of the specimen and the strain is strongly dependent on r_1/r_2 which complicates calculation of the local shear strain from the displacement.

Since very small variations in the value of r_1 and r_2 cause distinct changes in the specimen response, only the response of specimens manufactured with a high accuracy with respect to r_1 and r_2 are comparable.

Figure 14: Force-displacement curve for specimens with different shear region width

Changing r_1/r_2 affects the amount of material involved in the deformation process, stress homogeneity and the hydrostatic stress. Figure 15 represents the hydrostatic stress in the centre of the shear region as a function of r_1/r_2 at a displacement of 0.15mm. A shear band has not been developed yet at this stage of deformation for all specimens. The stress is always positive, even in specimens with $r_1/r_2 > 1$. Further

increasing r_1/r_2 in order to reduce the hydrostatic pressure (pure shear) is not useful because the stress distribution becomes very inhomogeneous for high r_1/r_2 -ratios.

Figure 15: Hydrostatic stress in the centre of the shear region at a displacement of 0.15mm as a function of the width of the shear region

Height of the shear region

Simulations are performed with heights of the shear region ($H = h_2 - h_1$) of 0.5mm, 1mm and 1.5mm. Besides the height, also the width (r_1/r_2) of the shear region was adapted in order to have the same angle of the geometric shear line (=line which connects the two corners). The force-displacement curves of these simulations are plotted in Figure 16.

The force is proportional to the height of the shear region because the amount of material involved in the shearing process is proportional too. In Figure 16 additional curves are presented where the force of the $H=1\text{mm}$ specimen has been scaled with a factor of 1.5 and 0.5. The resulting force-displacement curves show the same force levels as for the specimens with $H=1.5\text{mm}$ and $H=0.5\text{mm}$. However, scaling of only the force is not enough for the scaled curves to match with the original curves. Obviously, changing the height of the shear region also affects the displacement, yet unlike the force, no simple scaling factor can be used here to account for the height of the shear region. By increasing the height of the shear region, the width of the shear region raises automatically.

In the simulations discussed here large differences in height are considered. As shown in the previous section, small changes in the r_1/r_2 ratio result in a totally different specimen behaviour, which is not the case here. It can thus be concluded that the height of the shear region H is less influential than the width of the shear region r_1/r_2 .

Figure 16: Force-displacement curve for specimens with different shear region height

Radius of the corners

In the previously presented simulations, the corners of the specimen are sharp (radius $R=0\text{mm}$). However, the corners of a machined specimen will always have a certain rounding (see Table 2). To study the effect, simulations are performed with radii of the inner and outer corner of 0mm , 0.25mm and 0.5mm .

Results are presented in Figure 17. As can be seen, distinct differences exist in both force and deformation levels. A higher radius results in a higher force level. The maximum force reached in a specimen with sharp corners is almost 25% lower than the force reached in the $R=0.25\text{mm}$ specimen. A second effect of the radius is that the peak force is delayed; the rounded corners reduce the stress concentration significantly and therefore postpone strain localization.

Again, for reasons of comparison, the radius of the corners should be controlled tightly.

Figure 17: Force-displacement curves for specimens with different radius of the corners

4.3. From global to local behaviour

From measurements during an experiment the force corresponding to a certain deformation of the material sample can be calculated using equations 2.1 and 2.2. For an in-depth understanding of the material behaviour, it is important to know how this global response relates to stresses and strains in and around the shear zone in the material. FE simulations are used to assess whether or not an unambiguous relation between the global, measured response and the local material behaviour can be established.

Shear stress

Since the angle between of the geometrical shear line and the axial direction is small, the average shear stress in the shear zone can be approximated by the ratio of the axial force F_a and the surface of the shear band A_{SR} . The Shear Stress Ratio (SSR) is introduced as the ratio of the maximum shear stress (radius of Mohr's circle) in the centre of the shear region τ_{centre} and the average shear stress to the:

$$SSR = \frac{\tau_{centre} \cdot A_{SR}}{F_a} \quad (4.1)$$

A constant SSR indicates that the local shear stress is proportional to the applied force. If, furthermore, the SSR is close to one, the shear stress can be calculated from the force. The SSR is affected by both

the homogeneity of the shear stress and the hydrostatic stress in the shear region and is mainly determined by the ratio r_1/r_2 . In Figure 18 the SSR is represented for different r_1/r_2 -ratios.

Figure 18: Shear stress ratio as a function of the displacement for specimens with a different shear region width (r_1/r_2). The interval where strain localization is expected to happen is found for displacements between 0.15mm and 0.25mm.

At the onset of loading, stresses concentrate at the corners of the shear zone and the SSR has very small values. However, for all specimens, the SSR rapidly increases and a fairly constant value is reached until a shear band develops. When the shear band has fully developed, the top of the hat is driven as a wedge into the brim and the SSR further decreases. The curve for the specimen with $r_1/r_2=1$ is initially close to one but shows a peak at a displacement of 0.2mm, because of the non-uniform stress distribution in the shear zone.

From Figure 18, it can be concluded that the specimen with $r_1/r_2=0.975$ has the best performance: in the region of interest (start of loading until development of the ASB) the force is a good measurement for the shear stress (SSR close to 1) and the shear stress is quite homogeneous during the entire experiment. For specimens with smaller r_1/r_2 -ratios the hydrostatic pressure is much more important and, eventually, for very small r_1/r_2 -ratio the experiment is closer to a compression test than a shear test. For specimens with $r_1/r_2>0.975$, the hydrostatic stress is lower, but the shear stress is less homogeneous along the shear line. Consequently, the calculated average shear stress is not representative for actual shear stress in the centre of the shear zone.

Shear strain

Calculation of the local strain in the shear zone is less obvious. When the elastic deformation of the material adjacent to the shear zone is neglected, the indentation of the hat into the brim is equal to the relative displacement of the specimen ends Δu calculated by eq. 2.1. However, because of the varying width of the shear zone and the non-homogeneous strain distribution in this zone, the indentation cannot straightforwardly be converted to a strain value. Post-mortem inspection of specimens of interrupted experiments learned that material has been plastically deformed in a zone of a least 50 μm while the width of the shear band is only 5 á 10 μm .

Figure 19 gives the plastic shear strain e_{rz}^p in the centre of a specimen with $r_1/r_2=0.975$ as a function of the displacement Δu . The figure confirms that indeed no unambiguous relationship exists between applied displacement and the strain in the centre of the shear zone. As can be seen, the plastic shear is clearly not proportional to the displacement. At low displacements ($< 0.05\text{mm}$), the actual plastic strain is almost 0, only at the corners plastic deformation occurs. Between 0.05mm and ca 0.16mm , plastic strain increases approximately linearly. Afterwards, the local strain increases much faster, the strain concentrates in a smaller region. Once the force needed to compress the specimen decreases, spring back of the brim is reflected in a much steeper rise of the strain. Even higher deformations ($>0.25\text{mm}$) result in plugging of the hat into the brim.

Figure 19: Plastic shear strain e_{rz}^p in the centre of the shear region. The strain is clearly not proportional with the displacement

5. Conclusions

Experiments on Ti-6Al-4V

- Reproducibility of the experiments is low due to the high influence of the specimen dimensions and the existence of dimensional variations along the circumference of the specimen. Especially the width of the shear region and radius of the corners are very important. These observations are confirmed by the simulations. Hence, good control of the specimen production process is necessary.
- Experiments with hat-shaped specimens are easy to interrupt. In this way, the material structure is studied at different strain levels. The evolution of the shear band and the formation of cracks are observed by optical microscopy. Micro-cracks and micro-voids are initiated at different places along the shear band where a low hydrostatic pressure exists and they follow the same orientation of the grains. Large cracks are formed by a process of void growth and coalescence.
- Cracks can disappear if deformation of the material is continued. Crack surfaces are pressed together by the hydrostatic pressure and are *welded* together by the heat generated by friction. At first sight, the welds appear like shear bands but their origin is different.

Finite element simulations

- A high, geometry dependent hydrostatic pressure exists in the shear region. The conditions of a pure-shear and homogeneous stress state cannot be accomplished simultaneously.
- The plane where the maximal shear stress occurs, rotates during the experiment until the shear stress orientation is almost coincident with the geometric shear line, at the moment the adiabatic shear band is formed.
- The shear stress existing in the shear region can be extracted from the measured force, within certain limits of specimen dimensions. The relation between the force and the stress is studied by use of the Shear Stress Ratio (SSR). On the other hand, the local shear strain cannot be determined unambiguously.
- A specimen with the outer diameter of the hat slightly larger than the inner diameter of the brim is the best compromise between good homogeneity of the shear stress, measurability of the shear stress and a stress state as close as possible to pure-shear.
- High temperatures are reached in the shear band and also a very high cooling rate is observed when the deformation stops.

Acknowledgment

The authors would like to acknowledge the Interuniversity Attraction Poles Program phase 6 (IUAP) of the Federal Science Policy of Belgium and the partners of IUAP-VI (www.m3phys.be)

Bibliography

- [1] Bai Y, Dodd B. Adiabatic Shear Localization. 1992.
- [2] Meyer LW, Manwaring S. Critical adiabatic shear strength of low alloyed steel under compressive loading. In: Metallurgical Applications of Shock-Wave and High-Strain-Rate Phenomena. Marcel Dekker; 1986. p. 657-74
- [3] Bronkhorst CA, Cerreta EK, Xue Q, Maudlin PJ, Mason TA, Gray GT. An experimental and numerical study of the localization behavior of tantalum and stainless steel. *International Journal of Plasticity* 2006; 22 (7): 1304-35
- [4] Nemat-Nasser S, Isaacs JB, Liu MQ. Microstructure of high-strain, high-strain-rate deformed tantalum. *Acta Materialia* 1998; 46 (4): 1307-25
- [5] Kad BK, Gebert JM, Perez-Prado MT, Kassner ME, Meyers MK. Ultrafine-grain-sized zirconium by dynamic deformation. *Acta Materialia* 2006; 54 (16): 4111-27
- [6] Meyers MA, Xu YB, Xue Q, Perez-Prado MT, McNelley TR. Microstructural evolution in adiabatic shear localization in stainless steel. *Acta Materialia* 2003; 51 (5): 1307-25
- [7] Beatty JH, Meyer LW, Meyers MA, Nemat-Nasser S. Formation of controlled adiabatic shear bands in AISI 4340 high strength steel. 1990; 90
- [8] Couque H. A hydrodynamic hat specimen to investigate pressure and strain rate dependence on adiabatic shear band formation. *Journal De Physique IV* 2003; 110 423-28
- [9] Longere P, Dragon A, Trumel H, Deprince X. Adiabatic shear banding-induced degradation in a thermo-elastic/viscoplastic material under dynamic loading. *International Journal of Impact Engineering* 2005; 32 (1-4): 285-320
- [10] Li JR, Yu JL, Wei ZG. Influence of specimen geometry on adiabatic shear instability of tungsten heavy alloys. *International Journal of Impact Engineering* 2003; 28 (3): 303-14
- [11] Coghe F, Rabet L, Kestens L. Deformation mechanism of a commercial titanium alloy Ti6Al4V as a function of strain rate and initial texture. *J. Phys. IV France* 2006; 134 845-50
- [12] daSilva MG, Ramesh KT. The rate-dependent deformation and localization of fully dense and porous Ti-6Al-4V. *Materials Science and Engineering a-Structural Materials Properties Microstructure and Processing* 1997; 232 (1-2): 11-22
- [13] Lee WS, Lin CF. Plastic deformation and fracture behaviour of Ti-6Al-4V alloy loaded with high strain rate under various temperatures. *Materials Science and Engineering a-Structural Materials Properties Microstructure and Processing* 1998; 241 (1-2): 48-59
- [14] Macdougall DAS, Harding J. A constitutive relation and failure criterion for Ti6Al14V alloy at impact rates of strain. *Journal of the Mechanics and Physics of Solids* 1999; 47 (5): 1157-85
- [15] Rittel D, Wang ZG. Thermo-mechanical aspects of adiabatic shear failure of AM50 and Ti6Al4V alloys. *Mechanics of Materials* 2008; 40 (8): 629-35
- [16] Shih-Chieh L, Duffy J. Adiabatic shear bands in a Ti-6Al-4V titanium alloy. *Journal of the Mechanics and Physics of Solids* 1998; 46 (11): 2201-31
- [17] Xue Q, Meyers MA, Nesterenko VF. Self-organization of shear bands in titanium and Ti-6Al-4V alloy. *Acta Materialia* 2002; 50 (3): 575-96
- [18] Chwalik P, Klepaczko JR, Rusinek A. Impact shear-numerical analyses of ASB evolution and failure for Ti-6Al-4V alloy. 7th International Conference on Mechanical and Physical Behaviour of Materials Under Dynamic Loading 2003; 257-62
- [19] Saito F, Fujihata K, Hashiguchi T, Usui T, Tamura H. The influence of the mechanical properties of thin pure titanium plates on high strain-rate deformation. *Japanese Journal of Applied Physics Part 1-Regular Papers Short Notes & Review Papers* 2004; 43 (10): 7192-99
- [20] Lins JFC, Sandim HRZ, Kestenbach H, Raabe D, Vecchio KS. A microstructural investigation of adiabatic shear bands in an interstitial free steel. *Materials Science and Engineering a-Structural Materials Properties Microstructure and Processing* 2007; 457 (1-2): 205-18
- [21] Kolsky H. An investigation of the mechanical properties of materials at very high rates of loading. *Proceedings of the Physical Society* 1949; 62 676-700
- [22] Lee WS, Liu CY, Chen TH. Adiabatic shearing behavior of different steels under extreme high shear loading. *Journal of Nuclear Materials* 2008; 374 (1-2): 313-19
- [23] Guduru PR, Ravichandran G, Rosakis AJ. Observations of transient high temperature vortical microstructures in solids during adiabatic shear banding. *Physical Review E (Statistical, Nonlinear, and Soft Matter Physics)* 2001; 64 (3): 036128/1-28/6
- [24] Ranc N, Taravella L, Pina V, Herve P. Temperature field measurement in titanium alloy during high strain rate loading - Adiabatic shear bands phenomenon. *Mechanics of Materials* 2008; 40 255-70
- [25] Guduru PR, Rosakis AJ, Ravichandran G. Dynamic shear bands: an investigation using high speed optical and infrared diagnostics. *Mechanics of Materials* 2001; 33 (7): 371-402

- [26] Teng X, Wierzbicki T, Couque H. On the transition from adiabatic shear banding to fracture. *Mechanics of Materials* 2007; 39 (2): 107-25
- [27] Dey S, Borvik T, Hopperstad OS, Langseth M. On the influence of constitutive relation in projectile impact of steel plates. *International Journal of Impact Engineering* 2007; 34 (3): 464-86
- [28] Van Slycken J, Verleysen P, Degrieck J, Samek L, De Cooman BC. High-strain-rate behavior of low-alloy multiphase aluminum- and silicon-based transformation-induced plasticity steels. *Metallurgical and Materials Transactions a-Physical Metallurgy and Materials Science* 2006; 37A (5): 1527-39
- [29] Rosakis P, Rosakis AJ, Ravichandran G, Hodowany J. A thermodynamic internal variable model for the partition of plastic work into heat and stored energy in metals. *Journal of the Mechanics and Physics of Solids* 2000; 48 (3): 581-607
- [30] Longere P, Dragon A. Evaluation of the inelastic heat fraction in the context of microstructure-supported dynamic plasticity modelling. *International Journal of Impact Engineering* 2008; 35 (9): 992-99
- [31] Addessio FL, Johnson JN. Rate-dependent ductile failure model. *Journal of Applied Physics* 1993; 74 (3): 1640-48
- [32] Lodygowski T, Perzyna P. Numerical modelling of localized fracture of inelastic solids in dynamic loading processes. *International Journal for Numerical Methods in Engineering* 1997; 40 (22): 4137-58
- [33] Cescotto S, Li XK. Modelling of strain localization in a large strain context. *Structural Engineering and Mechanics* 1996; 4 (6): 645-53

List of figure captions

Figure 1: Sketch of a split Hopkinson pressure bar set-up

Figure 2: Hat-shaped specimen between Hopkinson bars. Arrows represent the displacement direction.

Figure 3: Specimen dimensions: $r_1=4.0\text{mm}$, $r_2=4.1\text{mm}$, $r_3=8\text{mm}$, $h_1=4.0\text{mm}$, $h_2=5.0\text{mm}$ and $h_3=8.0\text{mm}$, with indication of the 'shear region centre'. The figure is taken from [1].

Figure 4: Stress-displacement curves of the dynamic experiments Exp1-Exp9

Figure 5: Stress-displacement curves of a typical dynamic (Exp1) and quasi-static experiment (Exp10). The arrows indicate the displacements where other dynamic experiments were interrupted.

Figure 6: LOM image of fully developed adiabatic shear band (Exp7); the arrows show the direction of the displacement

Figure 7: Schematic representation and LOM micrographs of fracture process: a) grains are initially approximated to circles; b) deformation causes grains to elongate and rotate; micro-cracks with the same orientation as the grains are formed (Exp9); c) several micro-cracks are linked, the resulting crack surface looks fragmented. Twins are observed in the vicinity of the shear band.

Figure 8: LOM image of specimen with deformation limited to 0.2mm by a stopper ring. The crack at the corner of the specimen is clearly formed by a process of void growth and coalescence (Exp9).

Figure 9: Illustration of ABAQUS/Explicit finite element model showing the mesh and boundary conditions used in all simulations. Different variants for the geometry have been used.

Figure 10: Comparison of dynamic and static force-displacement curves from FE simulations and experiments with the same specimen geometry

Figure 11: Stress composition in the centre of the shear region for a specimen with the dimensions of figure 3: shear stress σ_{rz} , normal radial stress σ_{rr} and axial stress σ_{zz}

Figure 12: Stress state in the centre of the shear region represented by means of Mohr's circle at three different moments: before localization (20 μs), during localization (40 μs) and at a fully developed shear band (80 μs)

Figure 13: Hydrostatic pressure and temperature distribution along the shear line at two different moments for a specimen with dimensions of figure 3.

Figure 14: Force-displacement curve for specimens with different shear region width

Figure 15: Hydrostatic stress in the centre of the shear region at a displacement of 0.15mm as a function of the width of the shear region

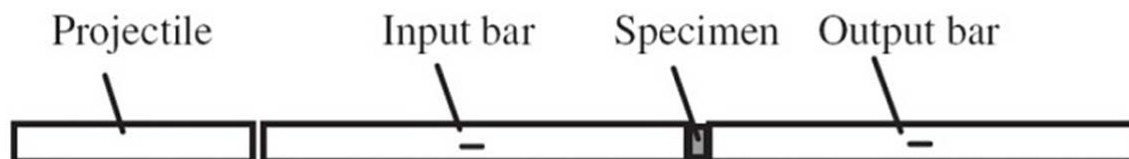
Figure 16: Force-displacement curve for specimens with different shear region height

Figure 17: Force-displacement curves for specimens with different radius of the corners

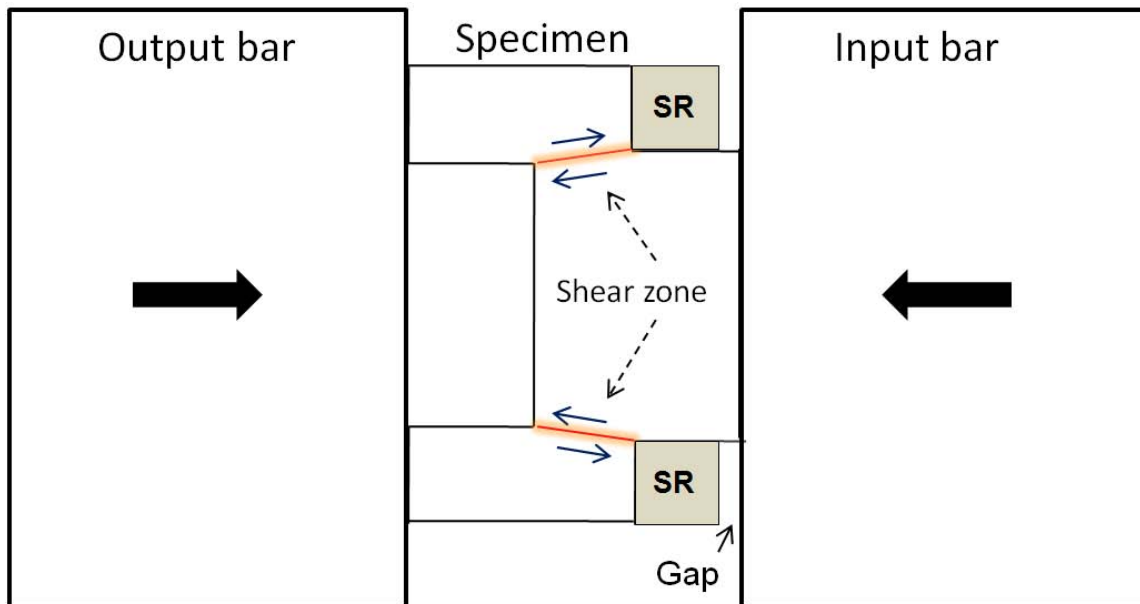
Figure 18: Shear stress ratio as a function of the displacement for specimens with a different shear region width (r_1/r_2). The interval where strain localization is expected to happen is found between a displacement of 0.15mm and 0.25mm.

Figure 19: Plastic shear strain e_{rz}^p in the centre of the shear region. The strain is clearly not proportional with the displacement

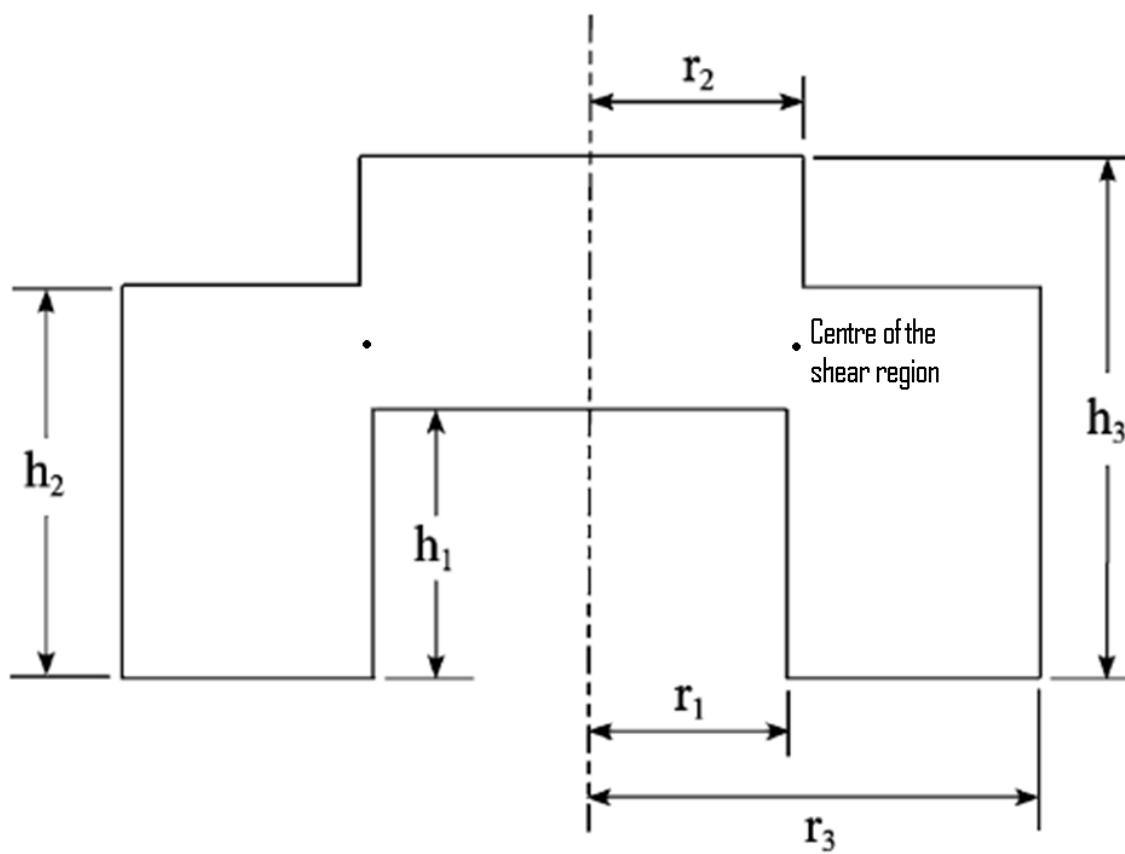
- [1] Bronkhorst CA, Cerreta EK, Xue Q, Maudlin PJ, Mason TA, Gray GT. An experimental and numerical study of the localization behavior of tantalum and stainless steel. *International Journal of Plasticity* 2006; 22 (7): 1304-35



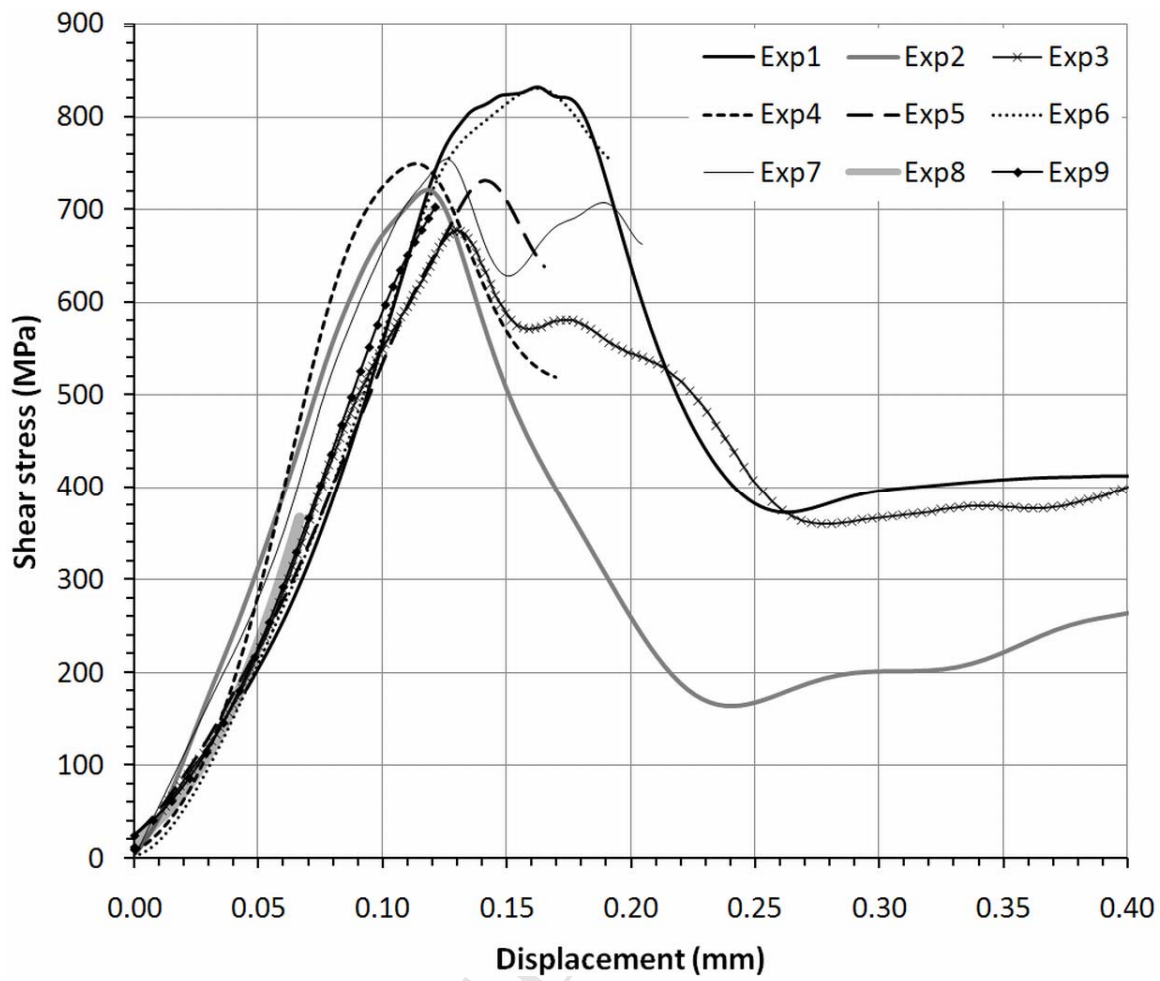
ACCEPTED MANUSCRIPT



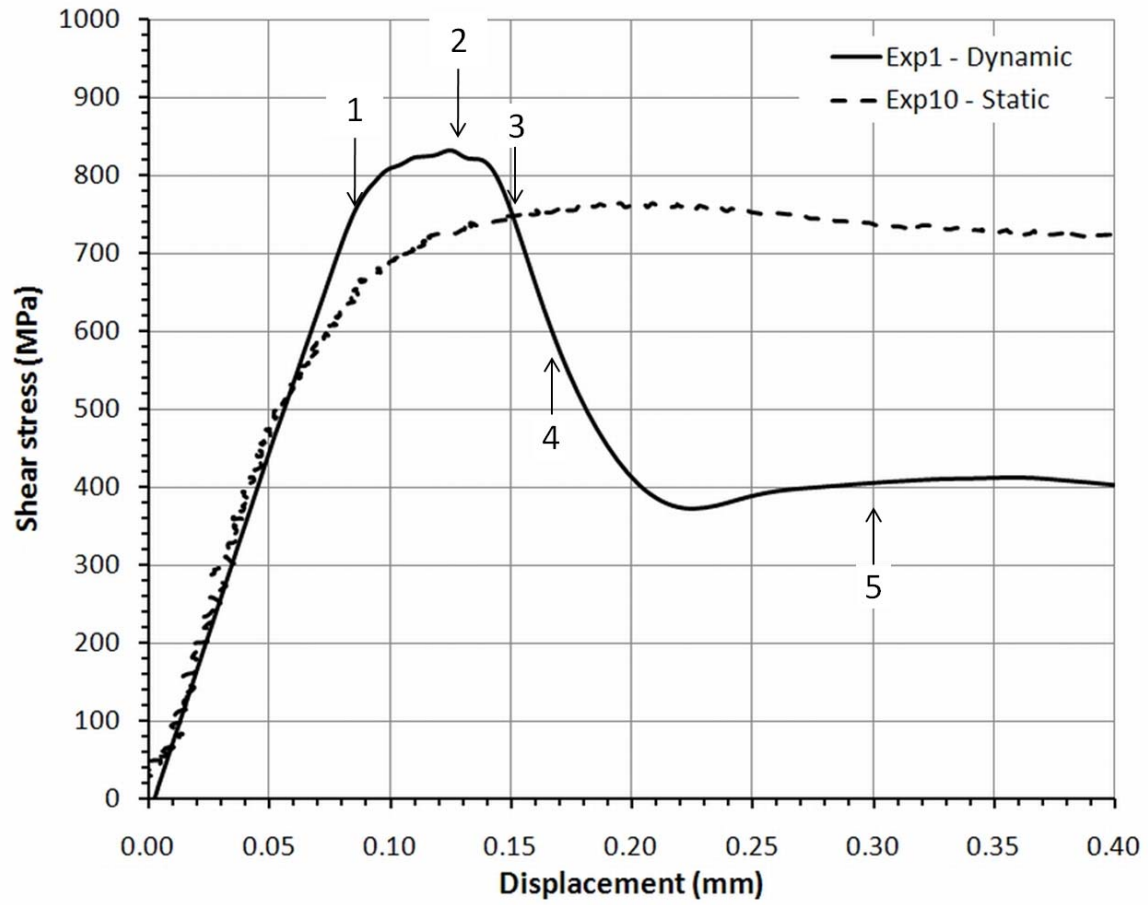
ACCEPTED MANUSCRIPT



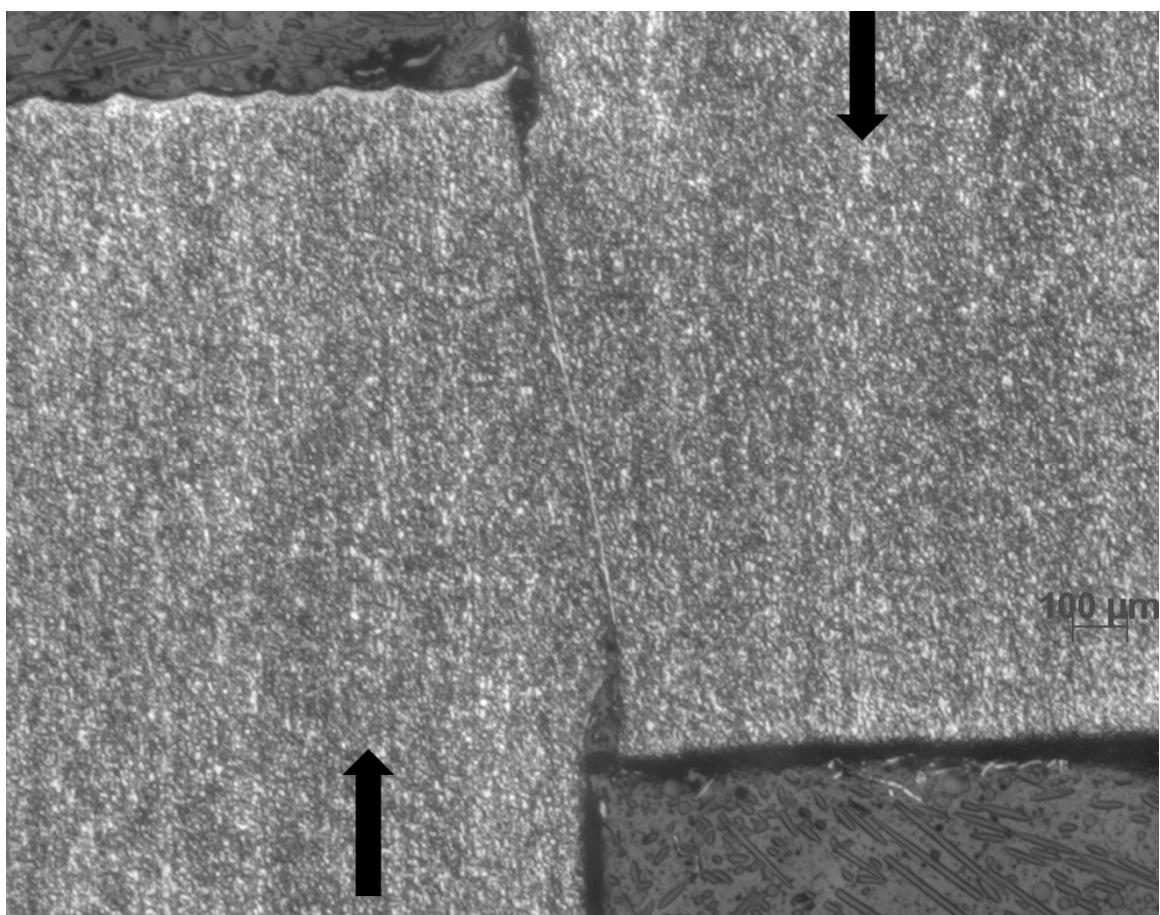
ACCEPTED MANUSCRIPT



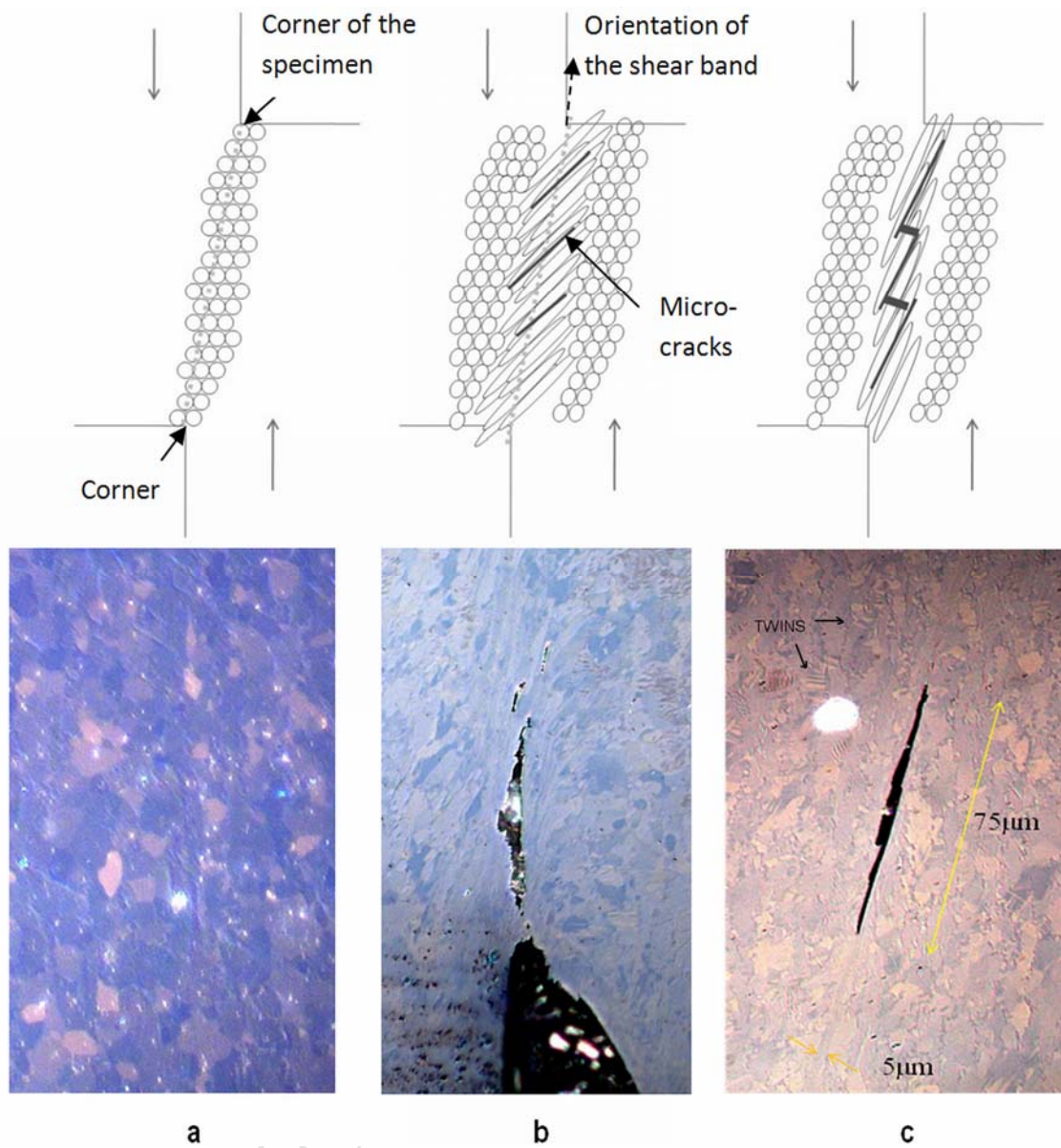
ACCEPTED

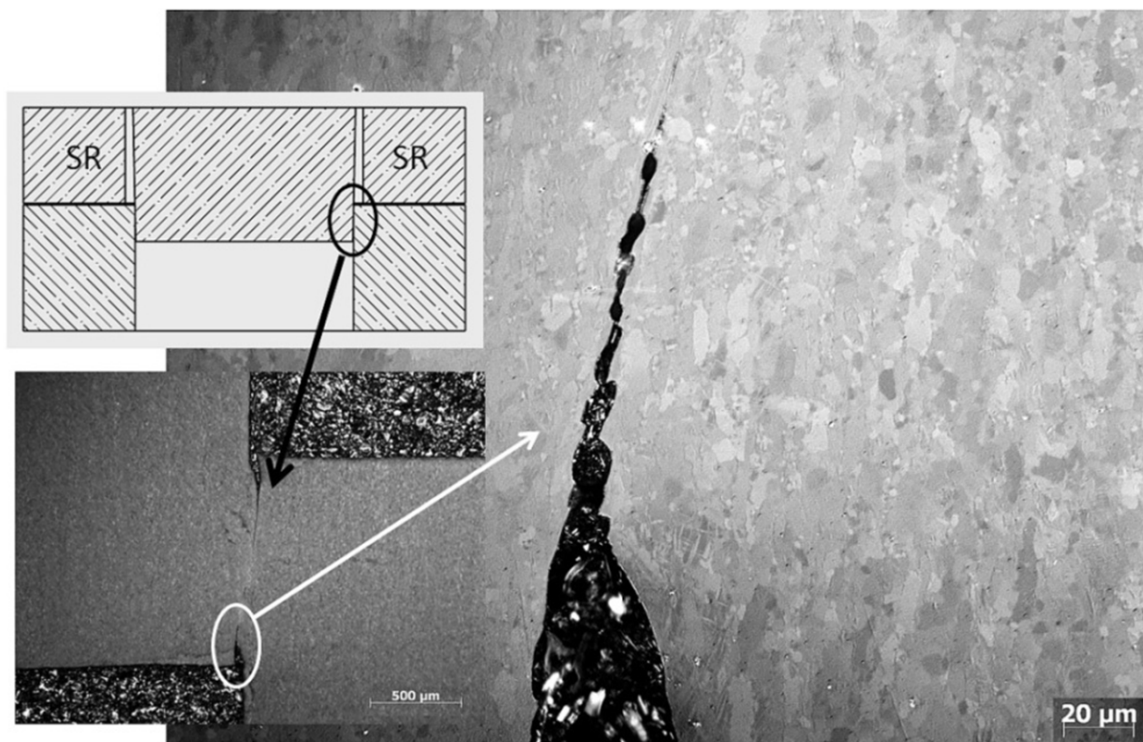


ACCEPTED

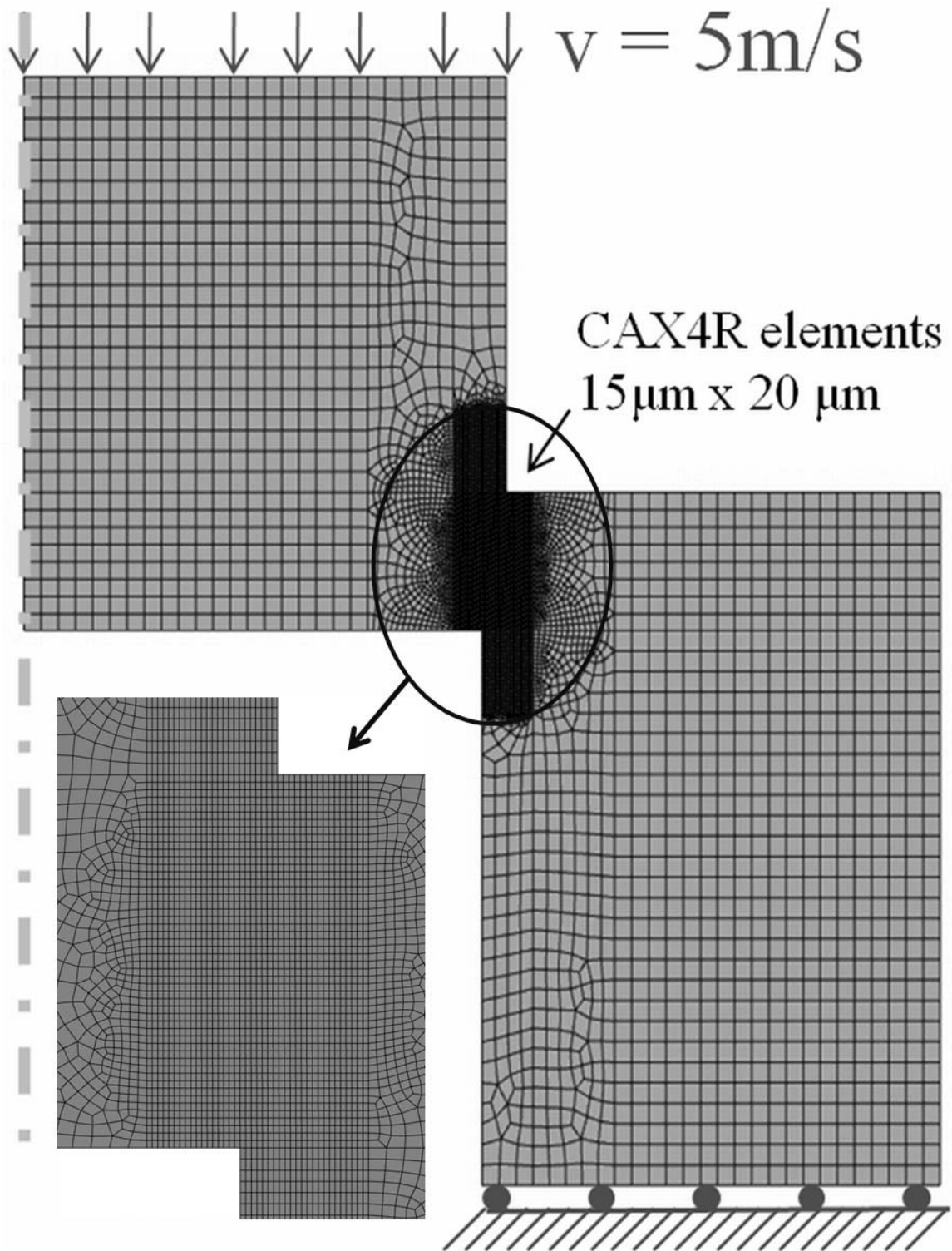


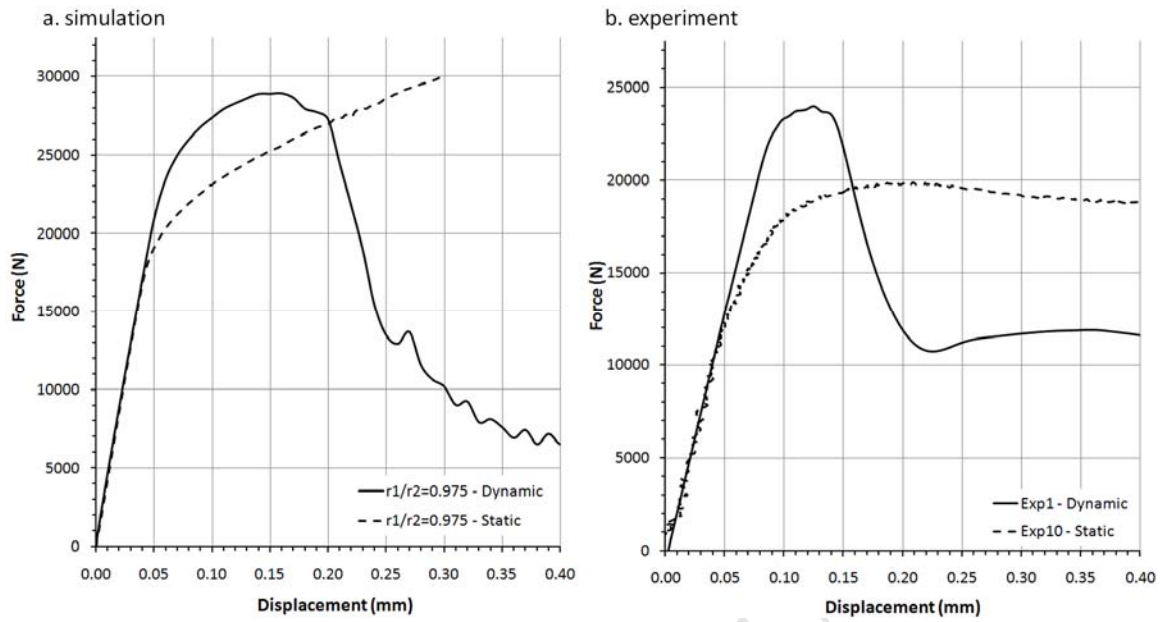
ACCEPTED

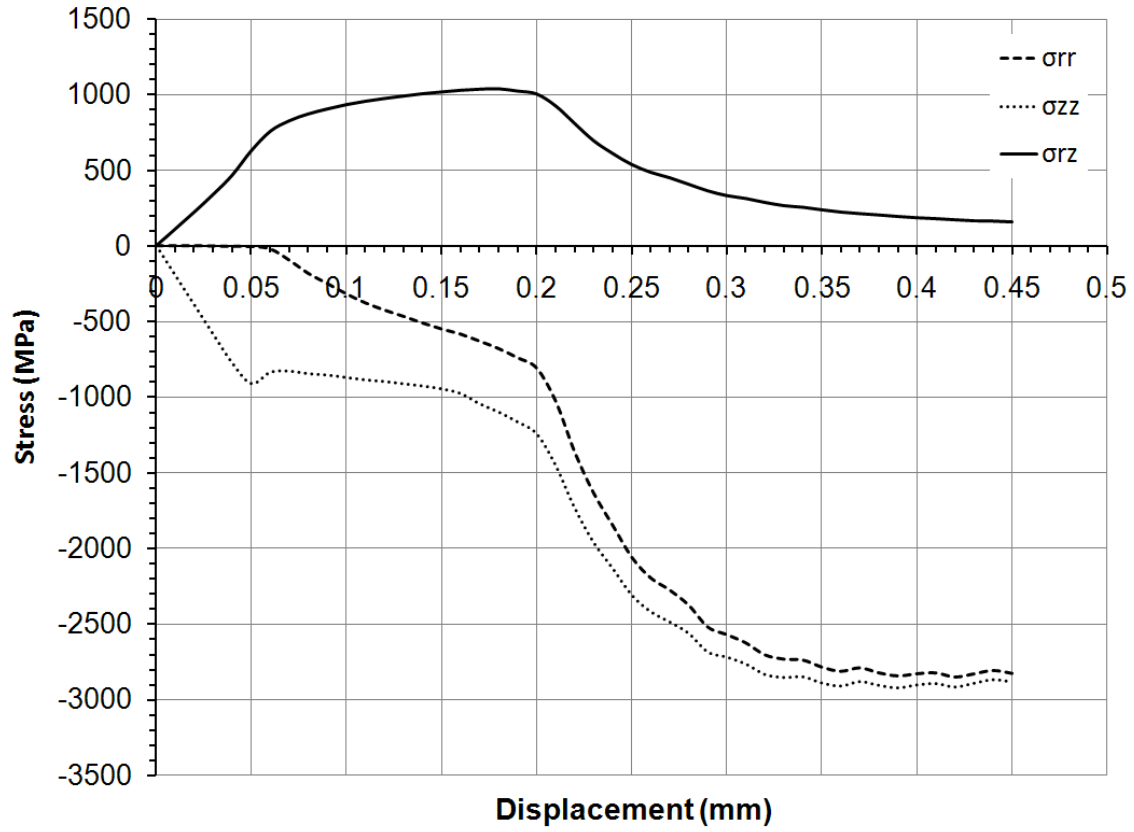




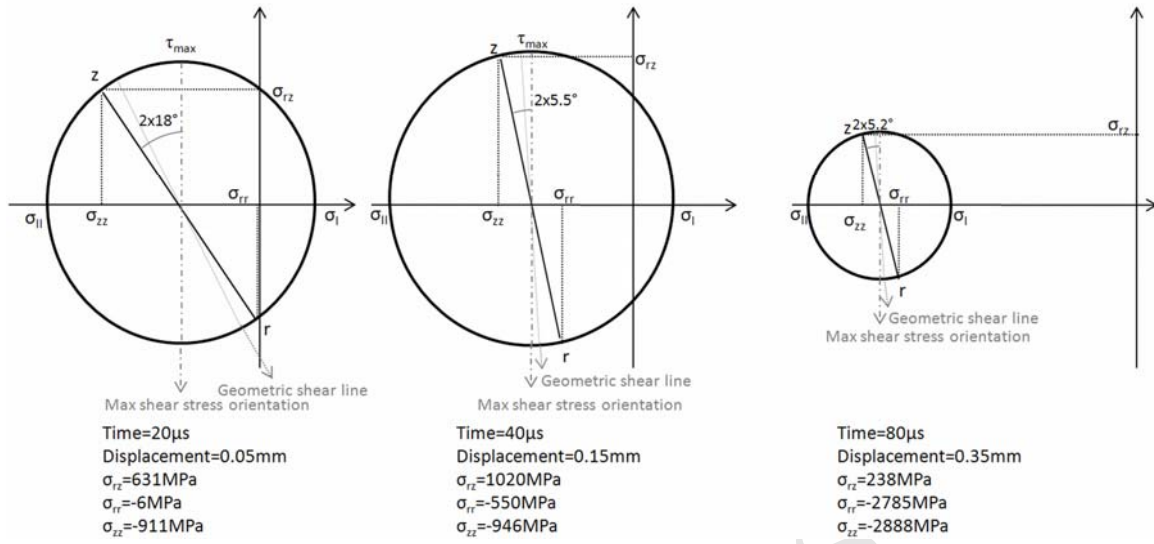
ACCEPTED MANUSCRIPT



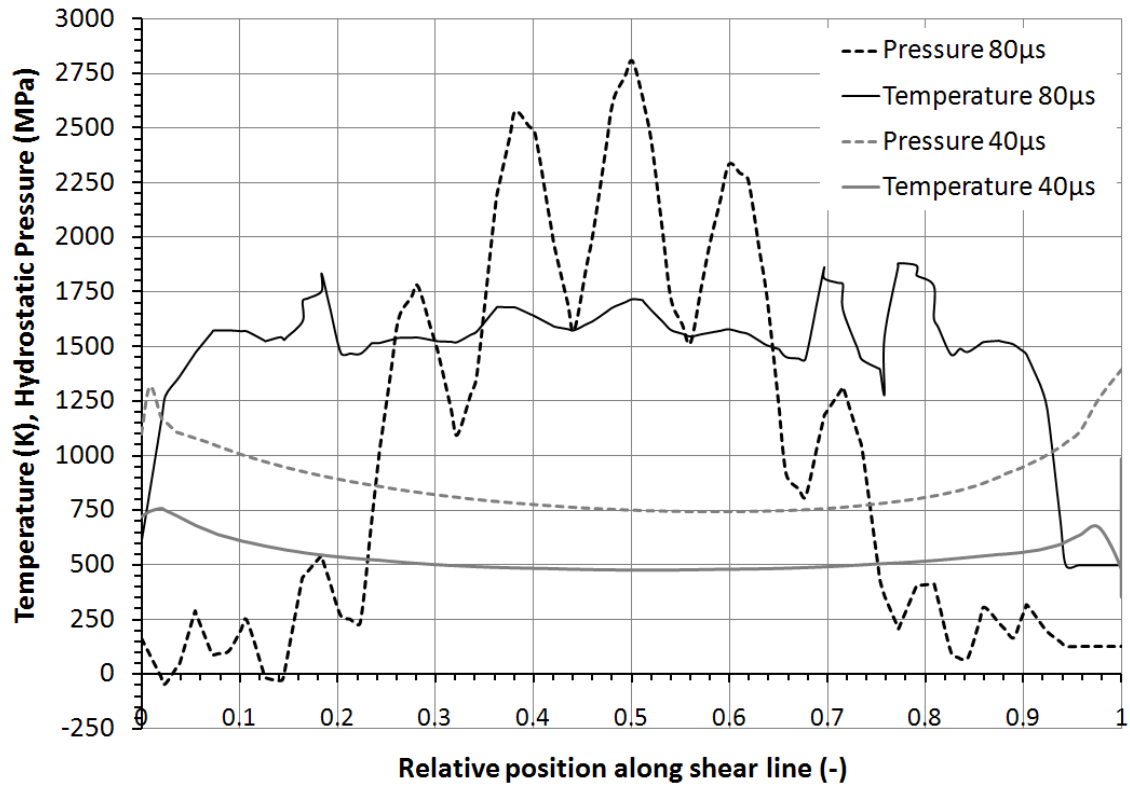




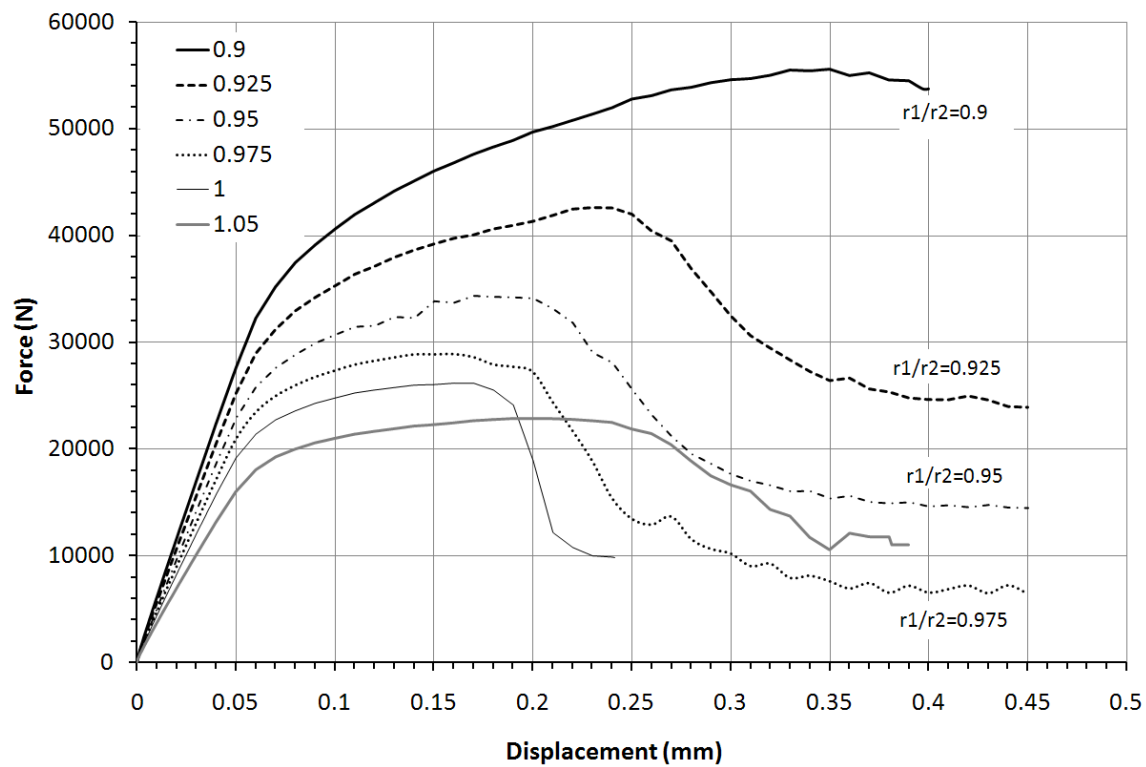
ACCEPTED MANUSCRIPT

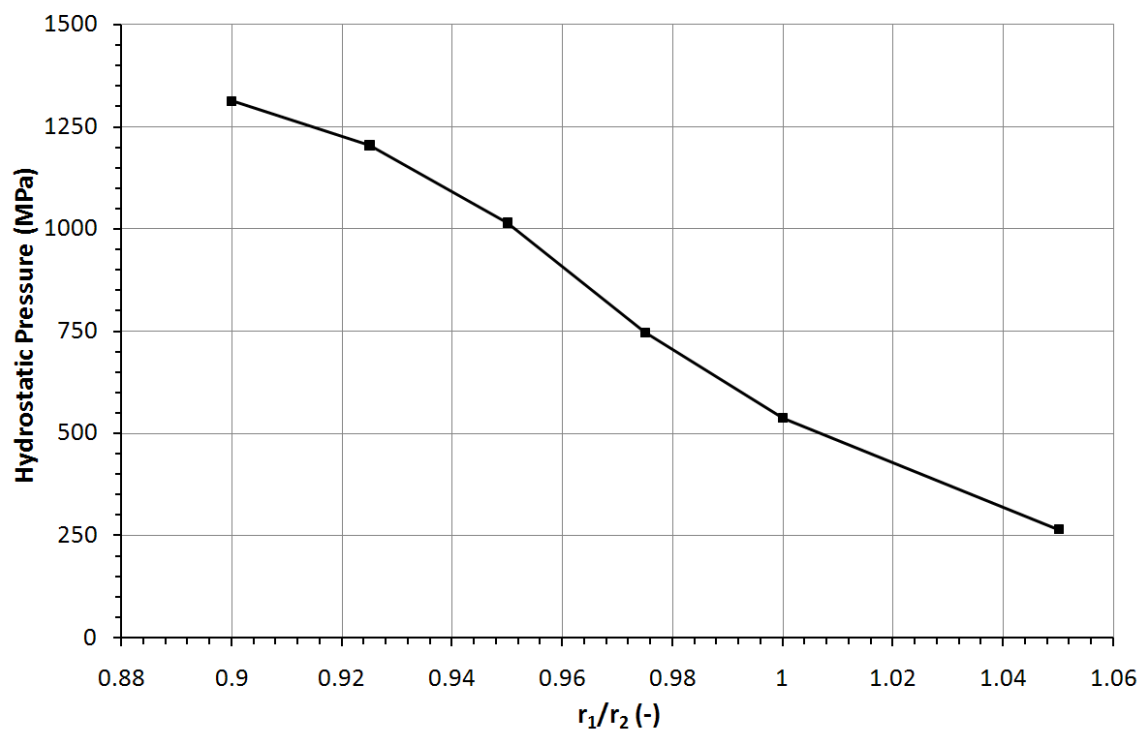


ACCEPTED MANUSCRIPT

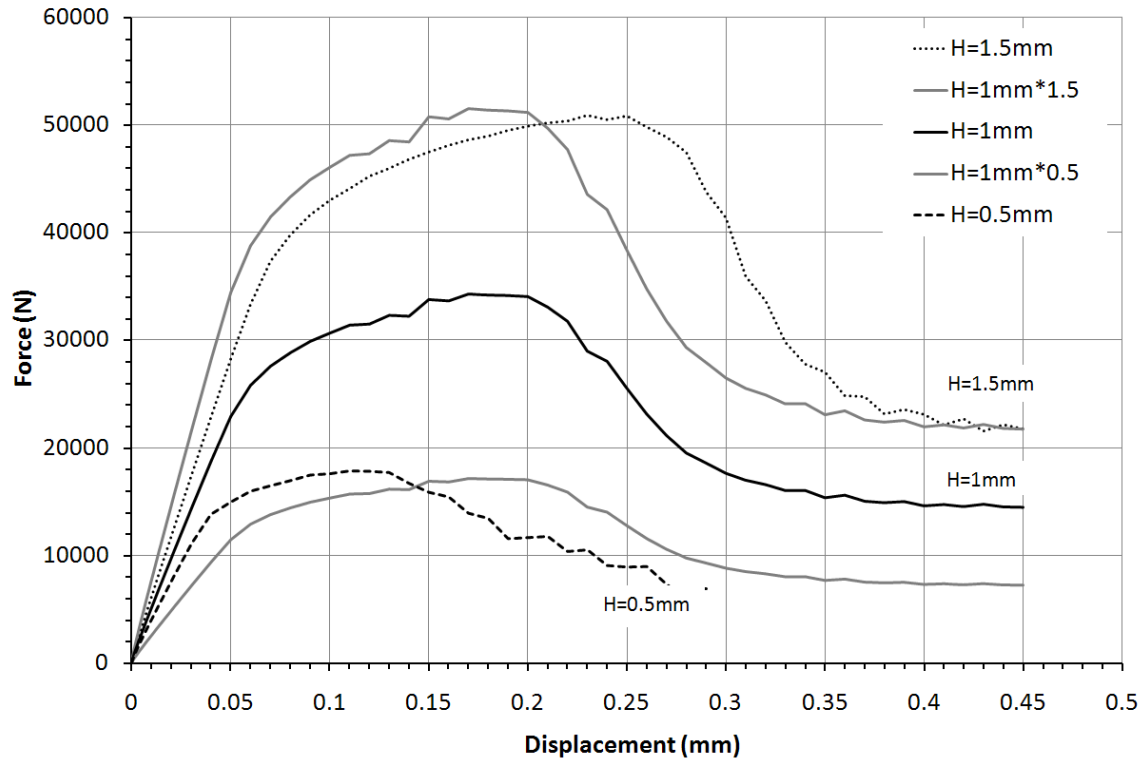


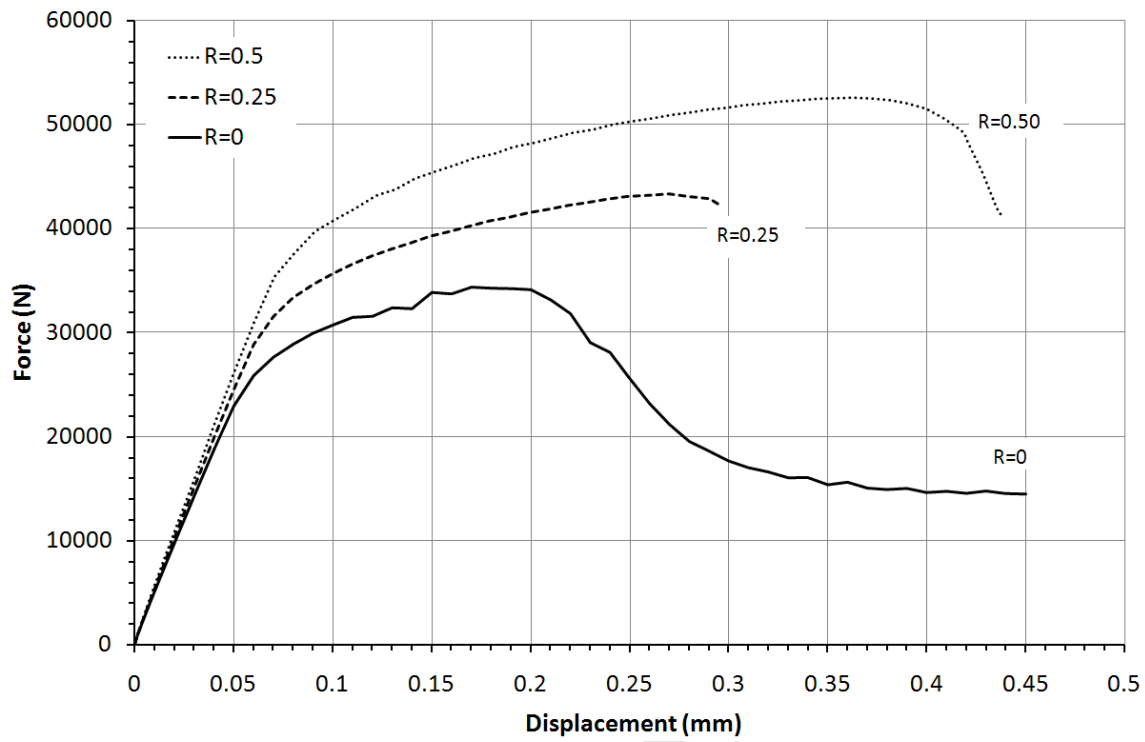
ACCEPTED MANUSCRIPT



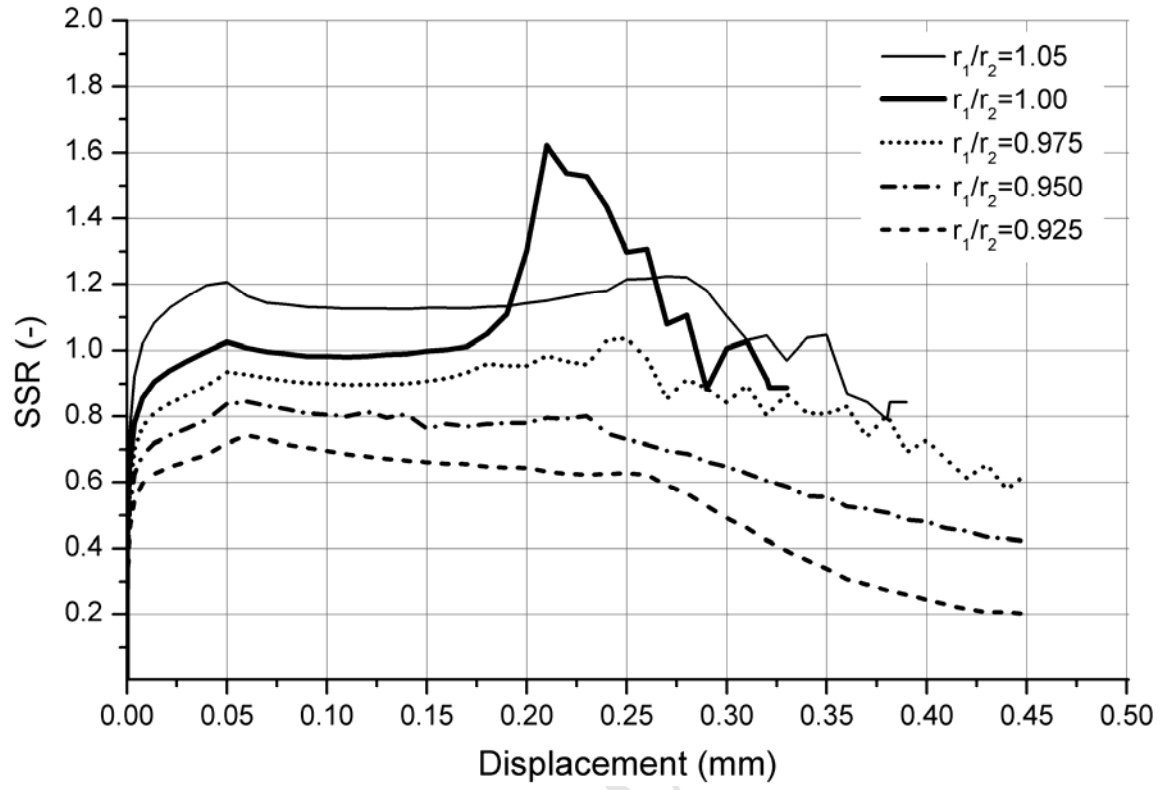


ACCEPTED MANUSCRIPT

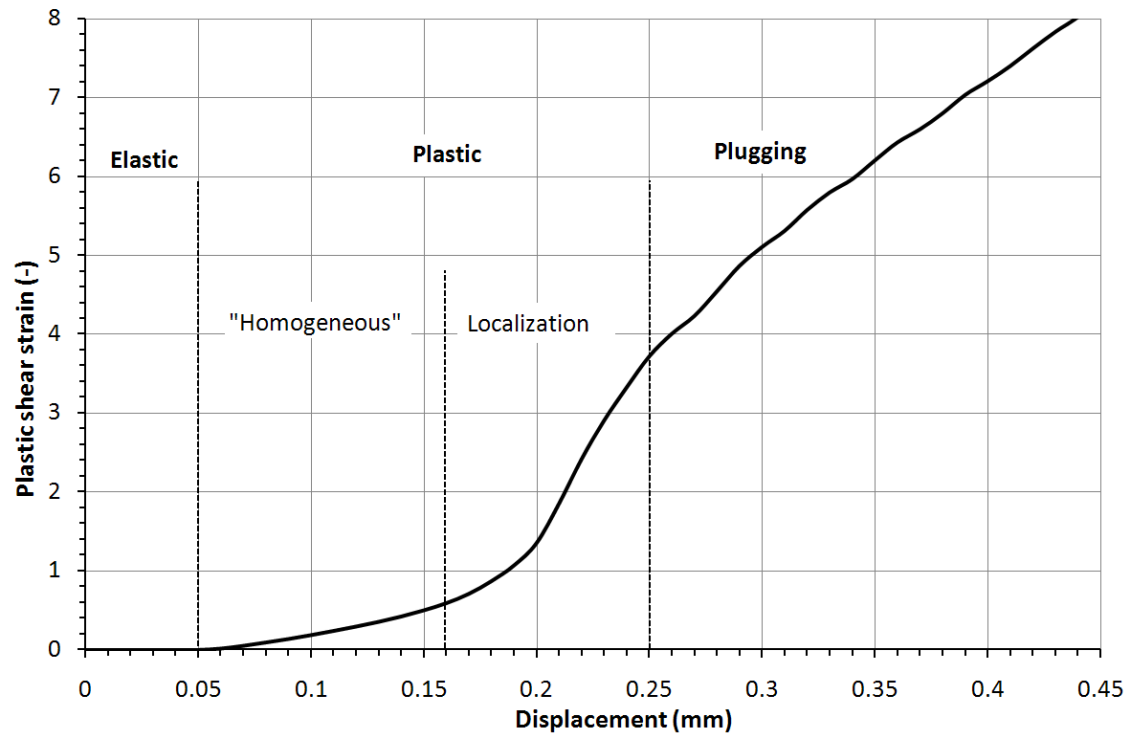




ACCEPTED MANUSCRIPT



ACCEPTED MANUSCRIPT



ACCEPTED MANUSCRIPT